Diffraction from Arrays of Plasmonic Nanoparticles with Short-Range Lateral Order

Markus Schwind,[†,*] Vladimir D. Miljković,[†] Michael Zäch,[†] Viktoria Gusak,[†] Mikael Käll,[†] Igor Zorić,[†] and Peter Johansson[†,‡]

[†]Department of Applied Physics, Chalmers University of Technology, SE-412 96 Göteborg, Sweden and [‡]School of Science and Technology, Örebro University, SE-70182 Örebro, Sweden

ABSTRACT We have measured the angular distribution of light scattered off 2D plasmonic Al nanoparticle ensembles. We created these samples with disk-like nanoparticles, 175 and 500 nm in diameter, respectively, using hole-mask colloidal lithography and electron beam lithography. The nanoparticle arrangements in the samples display the short-range order (but no long-range order) characteristic for an ensemble formed by random sequential adsorption. As a consequence of this, the ensemble scattering patterns can be quantitatively well described by combining the single-particle scattering pattern with a static structure factor that carries information about the diffraction effects caused by the short-range order of the ensemble. We also performed sensing experiments in which we monitored changes in the angle-resolved scattering intensity for a fixed wavelength as a function of the thickness of an ultrathin SiO_2 coating covering the Al nanoparticles. The data show that the angle and strength of the main diffraction peak vary linearly with SiO_2 coating thickness in the range 1.5–4.5 nm and suggest that measurements of the scattering profile could be a competitive alternative to traditional transmission measurements in terms of sensitivity.

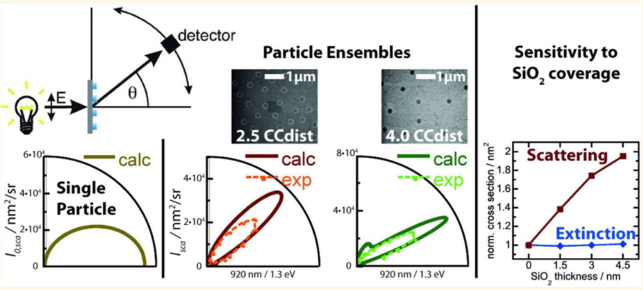

KEYWORDS: localized surface plasmon resonance · scattering · diffraction · nanoplasmonic sensing · signal enhancement · aluminum

Light scattering from metal nanoparticles is a topic with a long history,[1,2] which has attracted a lot of interest over the past decade within the field of nanoplasmonics. Experimentally, most studies aim at measuring the light scattered from single nanoparticles or structures of a few nanoparticles at a fixed range of angles.[3−5] However, in a few studies the total scattering cross section for various nanoparticles has also been measured. Using an integrating sphere, the total scattered light from a nanoparticle ensemble can be measured, and employing the optical theorem and normalizing by the particle density, the ratio of scattered and absorbed light for a single nanoparticle can be determined.[6−8]

The light-scattering properties of metal nanoparticles are important for a number of application areas. The performance of optical (plasmonic) nanoantennas,[9] which enable the manipulation and control of optical radiation at subwavelength scales, depends critically on the directional emission (scattering) from plasmonic nanostructures.[10−12] While this kind of study can be carried out with both a single nanostructure and an array of nanostructures, the antenna properties are usually set by the properties and geometry of the individual nanostructure.

Nanoplasmonic sensing is another application of nanoparticle light scattering in which great efforts have been made to develop and improve methods over the past decade. The goal of nanoplasmonic sensing is to detect the presence of foreign substances by measuring shifts of the localized surface plasmon resonance (LSPR) in metal nanoparticles.[13] Most studies aim at the detection of biomolecules,[13] but changes of material properties, such as phase transitions,[5,14] metal oxidation,[15,16] or metal hydride formation,[17] have been explored equally successfully.

* Address correspondence to markusschwind@gmail.com.

Received for review May 14, 2012 and accepted October 10, 2012.

10.1021/nn3021184

Independent of the field of application, nanoplasmonic sensing can be performed either on single nanoparticles or on nanoparticle ensembles. In single-nanoparticle measurements, the scattered light is measured using a dark-field microscope,[3−5] as the reflection from the substrate is generally too high for the small changes due to the interaction with the single nanoparticle to be observed. Measurements on single nanoparticles are usually performed when one is striving for the ultimate miniaturization of the sensor unit.

Ensemble measurements, on the other hand, exhibit a higher signal-to-noise ratio (S/N) and can be done with a simpler measurement setup. The nanoparticles used for sensing experiments are usually placed on transparent substrates, *e.g.*, glass, or dispersed in solution, and the measurements are typically performed in transmission geometry.[14,16−18] The nanoparticles can, however, also be placed on a reflective substrate, *e.g.*, a Si wafer, and nanoplasmonic sensing can be performed in reflection instead.[19−24] Comparing nanoplasmonic sensing on Au nanoparticles in transmission and reflection geometry, Svedendahl *et al.*[22] find a similar refractive index sensitivity for both geometries. Kedem *et al.*[23] even observe an up to 180% higher refractive index sensitivity for the reflection geometry, depending on the sample morphology. In a recent study, Shegai *et al.* investigated the wavelength-specific directional scattering or "color routing" from bimetallic nanoparticle dimers.[25] This phenomenon was subsequently utilized to realize a simple self-referenced single-wavelength detection scheme for hydrogen gas sensing,[26] combining the sensing and antenna properties of metallic nanoparticles. It was also recently shown that the specular reflection spectra from layers of plasmonic nanoparticles can exhibit dramatic angular dependences due to a Fano interference effect, a phenomenon of potential importance in sensing experiments.[27]

Intrigued by these recent results, we became interested in the angular dependence of the diffuse light scattering from two-dimensional nanoparticle ensembles and in the possibility of utilizing this effect in novel sensing modalities. In this paper, instead of looking at scattering from single nanoparticles, we study the angle-dependent scattering from short-range-ordered nanoparticle ensembles, which are often used for sensing measurements.[7,8,12,14,16,17,22,25] Apart from the dipolar LSPR peak, we observe diffraction peaks from the short-range-ordered nanoparticle ensembles. This fundamentally interesting behavior turns out to be in good agreement with calculations of the angular scattering pattern from a single nanoparticle combined with the structure factor calculated for the nanoparticle ensemble. We then explore the possibilities of sensing measurements using the scattered (diffracted) light: This approach yields two new sensing observables and leads to an increase in sensitivity (*ca.* 70% higher S/N) in the presented proof-of-principle study. Furthermore, this approach enables us to spectrally shift the peak being monitored during the sensing experiment without changing sample properties such as the nanoparticle size or shape, the substrate material, or the illumination angle.

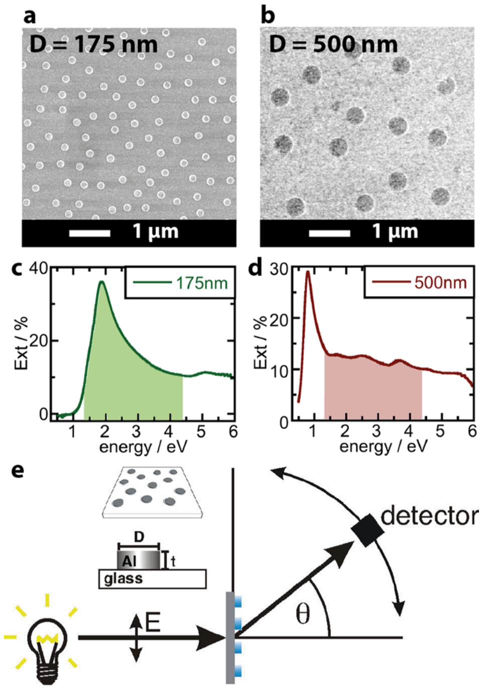

Figure 1. (a, b) SEM images of disk-like Al nanoparticles 175 and 500 nm in diameter, respectively, and 20 nm in height.[8] The nanoparticles have been fabricated by hole-mask colloidal lithography.[28] The arrangement of the nanoparticles can be described in terms of a random sequential adsorption mechanism.[29] The extinction spectra of the two samples are given in (c) and (d), as measured with a UV−vis−NIR spectrophotometer. The shaded area depicts the spectral range that can be measured using a standard UV−vis array spectrometer. This is the spectral range that we could access in our angle-dependent scattering measurements. (e) Measurement setup: white polarized light illuminates the sample from the back side. The detector (UV−vis array spectrometer) is moved at a constant distance from the sample in the plane spanned by the direction and the polarization of the incident light to detect angle-resolved scattering.

RESULTS AND DISCUSSION

Figure 1a and b show SEM images of the nanoparticles studied in this work, disk-like Al nanoparticles with a height of t = 20 nm and a diameter of D = 175 and 500 nm in diameter, respectively.[8] The nanoparticles have been fabricated by hole-mask colloidal lithography (HCL).[28] In HCL, polystyrene nanospheres are used to fabricate a hole-mask. The polystyrene nanospheres are commercially available with different diameters, which eventually determine the size of the Al nanoparticles. The negatively charged polystyrene nanospheres are adsorbed onto the positively charged mask surface, and due to the electrostatic interaction, they adhere to the surface while at the same time

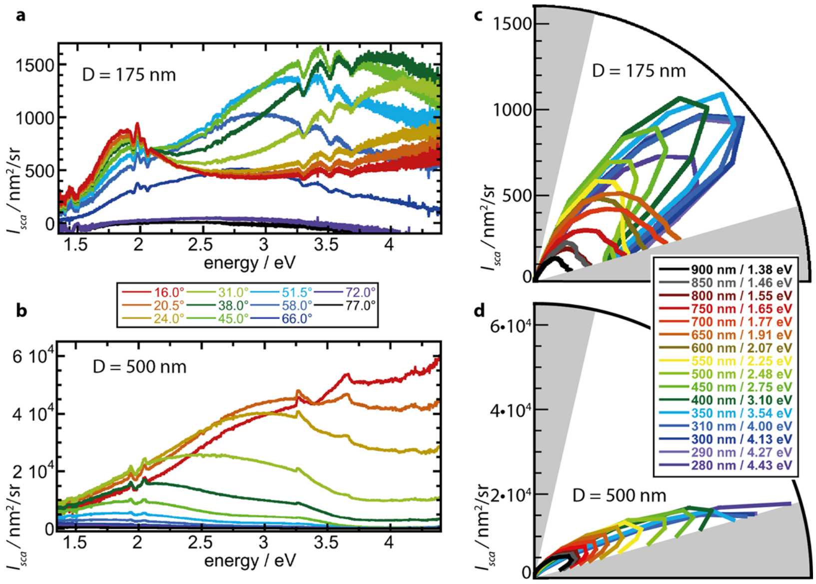

Figure 2. Experimentally measured scattering spectra taken at different angles for Al nanoparticles (a) 175 nm and (b) 500 nm in diameter fabricated by HCL (CCdist ~2.5). (a) At about 650 nm (1.9 eV), the dipolar LSPR can be seen. The broader peaks at higher energies (smaller wavelengths) are due to diffraction. Their peak position depends on the scattering angle. (b) For Al nanoparticles 500 nm in diameter, the dipolar LSPR peak falls outside the measured spectral range. Only the diffraction peaks are visible. One can see how the diffraction peaks shift from high to low energies with increasing scattering angle. (c, d) Evolution of these angular scattering distributions with changing wavelength for Al nanoparticles 175 and 500 nm in diameter, respectively. The angular scattering distributions in (c) are determined by the dipolar LSPR peak and diffraction peaks. In (d), the angular scattering distributions are dominated by the diffraction peaks. Scattering at angles smaller than 16° and larger than 77° off-normal (shaded area) cannot be measured because of limitations of the experimental setup.

repelling each other. This has two important consequences: (i) Particles avoid each other and do not adsorb within a certain region around already adsorbed particles. This mutual exclusion is in the following described in terms of the minimum center-to-center distance (CCdist) between two particles. (ii) The surface is covered by a single monolayer of nanospheres only, as all further particles are repelled. This adsorption pattern of the nanospheres directly determines the arrangement of the Al nanoparticles after the fabrication is finished. The particle arrangement is thus the result of a self-avoiding random sequential adsorption mechanism,[29] which during HCL stops once the surface is saturated. This yields a particle arrangement that exhibits short-range order (but not long-range order),[30,31] and the equilibrium particle coverage is set by the strength and range of the electrostatic interaction between the polystyrene spheres.

The extinction spectra of these Al nanoparticle patterns, *i.e.*, the spectra determined in forward transmission geometry ($\theta = 0°$), are displayed in Figure 1c and d. The largest features are the dipolar LSPR peaks located at 650 nm (1.9 eV) and 1500 nm (0.8 eV) for 175 and 500 nm Al particles, respectively. At 830 nm (1.5 eV), a narrow interband transition in Al leads to a small increase of extinction (not visible on this scale). We choose to study Al, instead of Au or Ag, which are typically used for sensing applications as they exhibit sharper plasmon peaks, as even for high energies (short wavelengths) no other interband activity can be observed in the spectral range accessible by the used spectrometers. Even though Al generally exhibits broader plasmon peaks than Au or Ag, it may still be the first choice for some sensing applications: Large-scale applications may benefit from the low price and great abundance. Its different (surface) chemistry compared to noble metals can be of importance for applications in catalysis and/or corrosion science. The dipolar LSPR peak and multipolar degrees of freedom lead to an asymmetric and relatively broad peak shape with noticeable extinction even at higher energies than the resonance position of the dipolar LSPR mode. A detailed study of the contributions of the multipolar degrees of freedom lies outside the scope of this study.

The shaded area below the extinction spectrum depicts the spectral range of the array spectrometer used for angle-dependent scattering measurements. The dipolar LSPR peak for D = 175 nm nanoparticles falls into this range, but for D = 500 nm it is shifted into the near-infrared.

We have measured angle-dependent scattering from the Al nanoparticle ensembles using the setup sketched in Figure 1e (*cf.* Methods section for a detailed description of the measurement setup).

Figure 2a shows the scattering spectra taken at different angles for Al nanoparticles, 175 nm in diameter. At 1.9 eV (wavelength of about 650 nm), we see the dipolar LSPR. As expected, its intensity decreases with increasing scattering angle. At higher energies, there are broad peaks that shift in frequency with changing scattering angle. As we will see, these peaks are due to diffraction, caused by interference between the light scattered off of neighboring particles. This phenomenon has been looked at in other contexts such as in studies of light transport and coherent back scattering in liquid suspensions of light-scattering particles[32,33] with various degrees of short-range order and in biomimetic materials with a structural short-range order similar to that seen in bird feathers.[34]

Figure 2b shows spectra at different scattering angles for Al nanoparticles 500 nm in diameter. As previously stated, the dipolar LSPR peak falls outside the measured spectral range here, so only the diffraction peaks are visible. These peaks shift from high to low energies with increasing scattering angle. The small spikes seen in the scattering spectra are artifacts resulting from the fact that the baseline and the scattering measurements need to be taken at very different integration times. While they obviously influence the noise of the absolute value of the scattering amplitude, the noise of the ratio of scattered amplitude for different angles at a fixed photon energy is not affected. Therefore, the artifacts do not influence the shape of the angular scattering patterns shown in the following plots.

In order to visualize the angular dependence, the scattering amplitudes observed at different angles for a constant wavelength have been plotted in polar coordinates. Figure 2c and d show the evolution of these angular scattering distributions with changing wavelength for Al nanoparticles 175 and 500 nm in diameter, respectively. In the case of D = 175 nm, displayed in Figure 2c, both the dipolar LSPR peak and the diffraction peaks determine the angular scattering patterns. At the dipolar LSPR peak wavelength and longer wavelengths (smaller photon energies) these patterns are nearly identical in shape, falling off with increasing scattering angle θ, while the overall amplitude has a maximum at λ = 650 nm and decreases the longer the wavelength becomes. For wavelengths shorter than 650 nm, the angular scattering pattern changes considerably. It now exhibits a maximum for scattering angles around $\theta \approx 45°$.

The evolution of the angular scattering pattern for D = 500 nm Al nanoparticles with changing wavelength is displayed in Figure 2d. Here, the dipolar LSPR peak falls outside the detector measurement range (*cf.* Figure 1d), and all scattering peaks are due to diffraction. For the longest wavelength, λ = 900 nm, the scattering pattern exhibits a maximum at $\theta \approx 30°$, and, as can be expected of a diffraction effect, with decreasing λ this angle decreases continuously until it starts to overlap with the specular beam for λ < 350 nm and, therefore, no longer can be measured.

In order to differentiate between single-particle contributions and features arising from the ensemble, we have fabricated samples with different interparticle spacings, *i.e.*, minimum center-to-center distances (CCdist). Here, the CCdist is given in multiples of the diameter; that is, a CCdist of 2 means that the distance between the centers of two neighboring particles cannot be smaller than twice the diameter of a single particle, or equivalently the minimum free space between the particles cannot be smaller than one particle diameter.

By using e-beam lithography (EBL), we have fabricated random arrays of Al nanoparticles 500 nm in diameter, with different CCdist between particles. In EBL, virtually any 2D sample pattern can be predefined on the computer, which is then "written" onto the fabrication mask by a raster-scanned electron beam. In this work, we determine the nanoparticle positions on the substrate by a random sequential adsorption algorithm mimicking the natural self-assembly during the HCL process. The main difference is that the parameter defining particle spacing, the minimum center-to-center distance, can be easily set to any desired value, including large spacings, which can be difficult to realize using HCL. In this work we study arrays with three different CCdist, namely, CCdist = 2.5, 4.0, and 7.0. Figure 3a and b show SEM images for 2.5 and 4.0 CCdist arrangements, respectively. (SEM images for samples with a CCdist of 7.0 are not shown here, as the particle density is so low that SEM images are hardly informative.) For comparison, all samples fabricated by HCL in the context of this work exhibit a CCdist around 2.5.

In Figure 3c to v, experimental results from the three different EBL samples with different CCdist are compared with calculated angular scattering patterns of single particles and of the nanoparticle ensembles. The calculated scattering patterns for a single nanodisk ($I_{0,\mathrm{sca}}(\theta, \phi)$) were obtained by using a commercially available finite element method together with Green's function method. From the single-particle scattering pattern $I_{0,\mathrm{sca}}(\theta, \phi)$ and knowing the exact positions of all particles in the array (which is the case for the experimental EBL samples), the scattering patterns of the ensemble ($I_{\mathrm{sca}}(\theta, \phi)$) can be calculated as[35]

$$I_{\mathrm{sca}}(\theta, \phi) = |S(\theta, \phi)|^2 I_{0,\,\mathrm{sca}}(\theta, \phi) \tag{1}$$

where $|S(\theta, \phi)|^2$ is the structure factor. Here, we have assumed that the particles are well separated and driven only by the incident fields, which is a reasonable approximation for the interparticle distances investigated in the experiments. The structure factor is defined as $|S(\theta, \phi)|^2 = (\sum_{i=1}^{N} \mathrm{e}^{i\vec{q}\cdot\vec{r}_i})(\sum_{j=1}^{N} \mathrm{e}^{-i\vec{q}\cdot\vec{r}_j})$, where N is the number of particles, $\vec{q}$ is the in-plane wave vector, with $|\vec{q}\,| = k \sin(\theta)$. Averaging the structure factor over all particle distances we get

$$\langle |S(\theta)|^2 \rangle = N + \langle \sum_{i=1}^{N} \sum_{j \neq i} \mathrm{e}^{i\vec{\mathrm{q}}\cdot(\vec{\mathrm{r}}_i - \vec{\mathrm{r}}_j)} \rangle \tag{2}$$

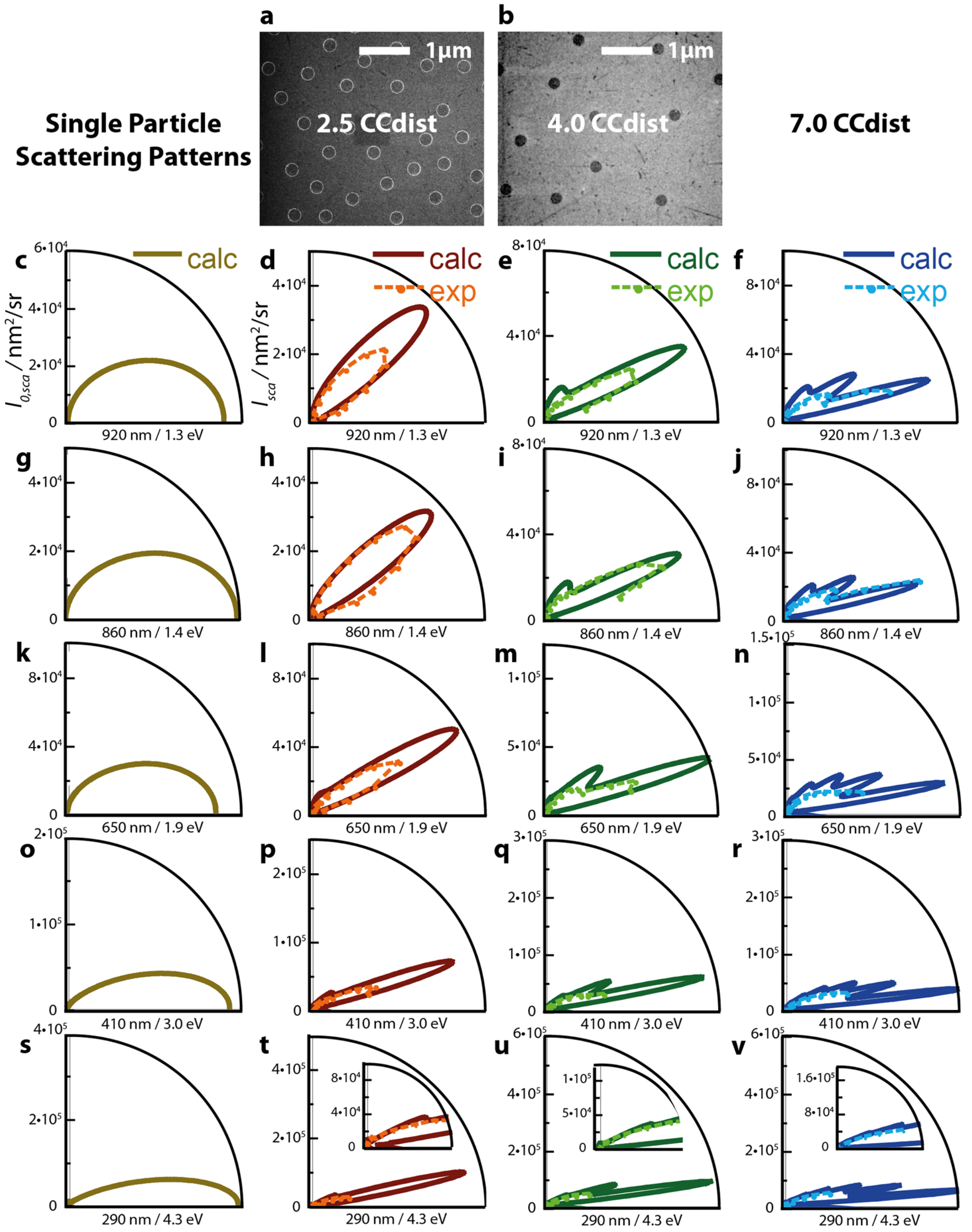

Figure 3. (a, b) SEM images of nanoparticle arrays created with EBL and a minimum center-to-center distance (CCdist) of 2.5 and 4.0, respectively. For a CCdist of 7.0, SEM images are hardly informative, as the spacing between the particles becomes very large. (c) Calculated single-particle scattering pattern. (d–f) Comparison between calculated and measured scattering patterns of the nanoparticle ensembles with 2.5, 4.0, and 7.0 CCdist, respectively, at 920 nm (1.3 eV). (g–v) The four corresponding scattering patterns for other wavelengths.

From this expression we find that the structure factor in the forward direction is $\langle|S(\theta)|^2\rangle = N^2$ and for $\theta \neq 0$ the structure factor can be calculated by an integration over interparticle distances r,

$$\langle\,|S(\theta)|^2\rangle = N\left[1+\frac{N}{A}\int_0^\infty (g(r)-1)J_0(qr)2\pi r\,\mathrm{d}r\right] \quad (3)$$

where A is the area of the sample, $J_0(qr)$ is a Bessel function, and $g(r)$ is the pair correlation function calculated from the experimentally given particle positions, as shown in ref 30. As an illustration, Figure 4 shows the pair correlation function for an array of particles made with EBL. In this case, as well as in Figure 8 of ref 30, $g(r)$ vanishes inside the correlation hole (where r is smaller

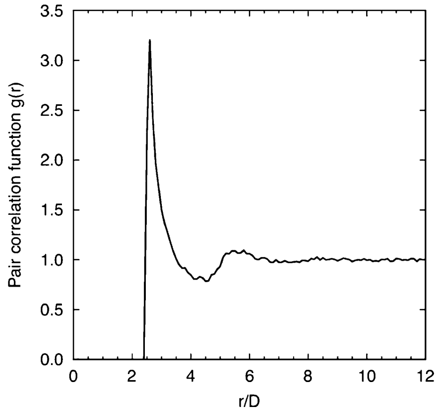

Figure 4. Pair correlation function *g*(*r*) as a function of the ratio *r*/*D* between the interparticle distance *r* and the particle diameter *D* = 500 nm for an array of nanoparticles created with EBL. The minimum interparticle distance is 2.5*D*, and the pair correlation function was determined by counting the number of particles in bins of width *D*/10, hence the small-scale fluctuations.

than the minimum CCdist), then exhibits a sharp peak followed by a weaker secondary maximum around twice the minimum CCdist. The pair correlation function for an array fabricated by HCL exhibits essentially the same features, but the fact that the correlation hole does not have a sharp edge makes the main maximum of $g(r)$ smoother, broader, and lower (see Figure 2b of ref 36). Since for large r the pair correlation function $g(r) \rightarrow 1$, it suffices to carry out the integration in eq 3 over a limited range of r. Using eq 3 together with eq 1, we have calculated the scattering patterns for $\phi = 0$ for short-range-ordered particle arrays composed of N = 27 302 particles, as shown in Figure 3. Depending on the value of CCdist, these scattering patterns exhibit one or several maxima. They appear close to the same angles $\theta = \arcsin(n\lambda/a)$, $n = 1, 2, ...$, as where the maxima of the diffraction pattern generated by two scatterers (or two slits in a double-slit experiment), separated by a distance a equal to the CCdist, would occur. The maxima in the present scattering patterns have a certain width that is a manifestation of the fact that the array is not periodically ordered; if it were, the scattering pattern would consist of a series of sharp Bragg peaks.

As can be seen in Figure 3, the experimental and calculated scattering patterns agree very well. The absolute values of I_{sca} are often a bit smaller in the experiment than in the calculation; however, this can be attributed to inhomogeneous broadening, as no matter how good the fabrication process, the different nanoparticles of an ensemble always show slight variations of their properties such as size and shape. This is also a reason for why sharp scattering features are not reproduced equally well in the experiment as predicted in the calculations. For angles smaller than 16°, no experimental data can be obtained due to overlap with the specular beam. Nevertheless, the fact that we are able to describe the complex scattering patterns of nanoparticle ensembles by combining simulations of the LSPR response for a single nanoparticle with diffraction theory shows that the peaks observed are in fact due to diffraction. Experimentally, we have limited our study to the short-range-ordered nanoparticle ensembles as which are typically formed by HCL, due to the importance of nanoparticle ensembles formed by HCL for sensing applications. Our theoretical approach and EBL fabrication are, however, generic and therefore valid for any kind of nanoparticle ensemble (as long as interparticle distances are large enough to prevent near-field interaction between the particles).

In order to explore the potential of angular scattering measurements for nanoplasmonic sensing applications, an ensemble of Al nanoparticles, 175 nm in diameter and 120 nm in height (fabricated by HCL; CCdist ~2.5; the height has been increased in order to obtain larger scattering cross sections, which considerably shortens the time for angular scattering measurements), has been sputter-coated in three steps with ~1.5 nm of SiO_2 per step. We have measured extinction and scattering for the uncoated Al nanoparticle ensembles as well as for coatings of 1.5, 3.0, and 4.5 nm SiO_2.

The extinction spectra are shown in Figure 5a. The dipolar LSPR peak can be seen at 1.9 eV (650 nm; blue arrow). This peak red-shifts and the extinction cross section σ_{ext} increases slightly as the Al nanoparticles are coated with SiO_2. The changes of σ_{ext} are relatively small compared to the absolute value of σ_{ext}.

Figure 5b shows the scattering spectrum detected at an angle $\theta = 45°$ off-normal. The dipolar LSPR mode at 1.9 eV (green arrow) is still visible as a peak, but at higher energies (smaller wavelengths) the differential scattering cross section I_{sca} is much larger with a maximum $I_{sca,max}^{\theta=45°}$ at about 3.5 eV (350 nm; red arrow). As is described above, this is due to diffraction from the nanoparticle ensemble. It becomes obvious comparing Figure 5a and b that the relative changes for different coating thicknesses are much larger at θ = 45° than for the standard extinction measurement at θ = 0° even though the measurements have been performed on the same sample so exactly the same changes are sensed. As stated previously, the small spikes in the scattering spectra are artifacts due to the fact that the baseline and the scattering measurements need to be taken at very different integration times.

The spectral shift of the dipolar LSPR peak at $\theta = 0°$ and the maximum scattering peak at θ = 45° are compared in Figure 5c. The peak observed at 3.5 eV shifts about 4–5 times more than the dipolar LSPR peak in extinction as a result of SiO_2 coverage.

Figure 5d shows the changes of σ_{ext} (blue markers) and I_{sca} (red markers) at their maxima, *i.e.*, ~1.9 and ~3.5 eV, at $\theta = 0°$ and 45°, respectively, normalized to the absolute value of each cross section without SiO_2.

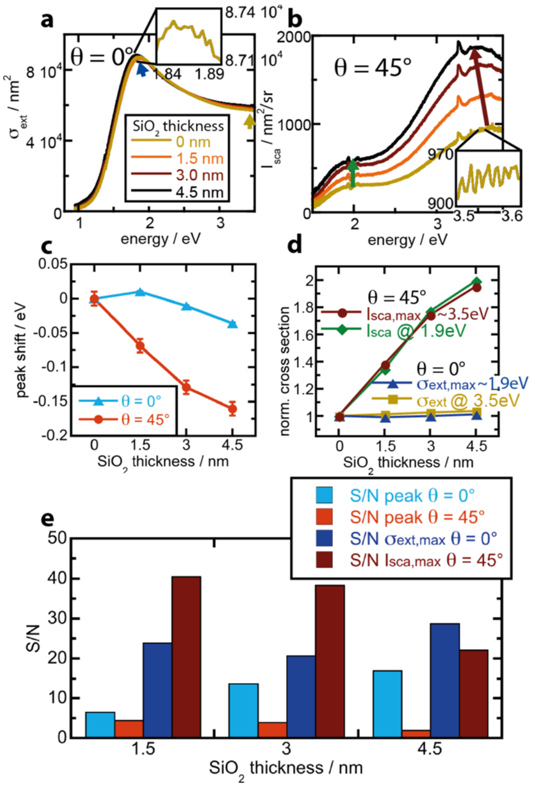

Figure 5. (a) Extinction spectra (θ = 0°) for an Al nanoparticle ensemble (fabricated by HCL; CCdist ∼2.5) covered with 0, 1.5, 3.0, and 4.5 nm of SiO_2. (b) Differential scattering cross sections per particle I_{sca} at θ = 45° for the same samples. The blue and red arrows in (a) and (b) indicate how the dipolar LSPR peak and the maximum in scattering $I_{sca,max}^{\theta=45°}$, respectively, shift when the nanoparticles are covered with SiO_2. The yellow arrow in (a) displays how the extinction cross section changes at the spectral position where $I_{sca,max}^{\theta=45°}$ occurs. The green arrow in (b) marks the shifts of I_{sca} at the dipolar LSPR position. (c) Comparison between the shifts of the dipolar LSPR peak as well as the maximum scattering peak at θ = 45°. (d) Comparison between the changes of σ_{ext} (blue markers) and I_{sca} (red markers) at their maxima, *i.e.*, ∼1.9 and ∼3.5 eV, at $\theta = 0°$ and 45°, respectively, normalized to the absolute value of each cross section without SiO_2. In addition, the normalized changes of the values of I_{sca} (θ = 45°) at the dipolar LSPR position (1.9 eV; green markers) and of the values of σ_{ext} (θ = 0°) at the spectral position, where $I_{sca,max}^{\theta=45°}$ occurs (3.5 eV; yellow markers), are shown. The color coding is the same as introduced by the arrows displayed in (a) and (b). As can be seen, the scattering cross section I_{sca} experiences a larger relative change than the extinction cross section irrespective of the photon energy. (e) Signal-to-noise ratios (S/N) for the four different observables shown in (c) and (d) and the three SiO_2 coating thicknesses. The color coding matches the respective colors in (c) and (d).

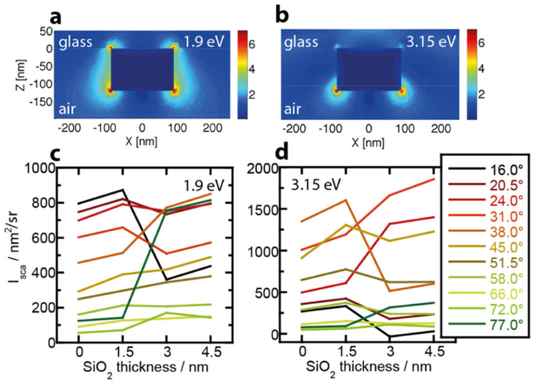

Figure 6. (a, b) Calculated electric field enhancement around a single Al nanoparticle at 1.9 eV (the dipolar LSPR position) and 3.15 eV (where $I_{sca,max}^{\theta=const}$ occurs in the calculation), respectively. (c, d) I_{sca} as a function of increasing SiO_2 thickness for different scattering angles at 1.9 and 3.5 eV, respectively. As can be seen, the scattering cross section varies in a nonmonotonic way with the SiO_2 thickness.

In addition, the normalized changes of the values of I_{sca} (θ = 45°) at the dipolar LSPR position (1.9 eV; green markers) and of the values of σ_{ext} ($\theta = 0°$) at the spectral position, where $I_{sca,max}^{\theta=45°}$ occurs (3.5 eV; yellow markers), are shown. At $\theta = 45°$, deposition of 4.5 nm SiO_2 almost doubles I_{sca} at both 1.9 and 3.5 eV, while at θ = 0°, in extinction, σ_{ext} increases only by a little more than 1% at each of these photon energies.

While large relative changes of the signal in response to the SiO_2 coverage are very promising in terms of enhancement of the sensing signal, the more important factor for sensing is the signal-to-noise ratio. The noise for all peak shifts and cross section shifts has been obtained from the measurements shown in Figure 5a and b, respectively (*cf.* insets). The maximum deviation from a smoothed average spectrum has been used as a measure of the noise of the extinction and scattering cross sections. This is to be compared with the signal, namely, the change of the extinction or scattering cross section as a result of coating the Al nanoparticle with SiO_2. This signal is normalized to a change of coating thickness of 1 nm. To determine the peak shift noise, we isolate a narrow wavelength range within which, considering the noise level, the maximum of the scattering or extinction cross section must be situated. We use the center of this wavelength range to define the peak position, and the width of the range to define the peak position noise. Figure 5e displays the S/N for the different sensing observables. A S/N of as high as 41 has been obtained for $I_{sca,max}^{\theta=45°}$. $\sigma_{ext,max}$ features a S/N of 24 for the thinnest SiO_2 coating and 29 for the thickest. As can be seen, the S/N of $I_{sca,max}^{\theta=45°}$ greatly exceeds the S/N of $\sigma_{ext,max}$ except for the thickest SiO_2 coating, for which $\sigma_{ext,max}$ actually exhibits a slightly larger S/N than I_{sca}.

The spectral peak shifts all show a lower S/N than the cross section changes. S/N = 5 is observed for the spectral shift of the maximum scattering peak for the thinnest SiO_2 coating, and S/N = 2 for the thickest SiO_2 coating. The dipolar LSPR peak shift measured at $\theta = 0°$ features a S/N = 7 for the thinnest and S/N = 17 for the thickest SiO_2 coating.

In the following, we consider the nature of the increased sensitivity of the angle-resolved scattering cross section. Figure 6a and b show the electric near-field enhancement variations at 1.9 eV (at the dipolar LSPR position) and 3.15 eV (where $I_{sca,max}^{\theta=45°}$ occurs in the calculations) in the *xz*-plane of a single nanoparticle. The near field has been calculated using a commercial finite element method. At 1.9 eV, the electric field enhancement is highest at the edges of the disk. The electric field is also enhanced along the sides of the disk. A considerable part of the enhanced field lies in the substrate. At 3.15 eV, the field enhancement is localized predominately around the edges of the disk extending into air. At this edge the magnitude of the field enhancement is about the same as at the dipolar LSPR position. Along the sides of the disk and around the edge on the substrate side, however, the electric field is hardly enhanced at all. As previously stated, a detailed study of the nature of the near field at higher energies lies outside the scope of this publication. Still, it is worth noting that the near field at higher energies is influenced by the tail of the dipolar LSPR resonance but also by higher order modes. In fact, the near field shown in Figure 6b arises from a mixed dipole and quadrupole mode.

Figure 6c and d show I_{sca} as a function of increasing SiO_2 thickness for different scattering angles at 1.9 and 3.5 eV, respectively. As can be seen, the scattering cross section in general varies nonmonotonically with the SiO_2 thickness.

So far, we have looked only at the changes at fixed angles. Figure 7 shows the full angular scattering pattern for the four different samples (Al nanoparticles covered by 0, 1.5, 3.0, and 4.5 nm of SiO_2). Figure 7a–e show the scattering patterns at different wavelengths. The addition of SiO_2 has a clear influence on them. In order to quantify the changes, the experimental data points have been fitted by a Gaussian function. Figure 7e shows the Gaussian fit in both polar and Cartesian coordinates (inset). The angles for which the maximum scattering cross sections at fixed wavelength are observed as well as these maximum scattering cross sections $I_{sca,max}^{\lambda=const}$ are related to the SiO_2 thickness in Figure 7f and g, respectively. In this particular thickness interval, both observables depend linearly on the SiO_2 thickness. The scattering angle increases by about 0.37° and the maximum scattering cross section $I_{sca,max}^{\lambda=const}$ by about 170 nm^2/sr per nanometer of SiO_2.

In addition to the traditional measurement of spectral peak shifts and changes in extinction and scattering amplitudes at a fixed angle, the measurement of angle-dependent scattering yields two more observables, which in this proof-of-principle study turn out to be a simple (due to the linear dependency) and sensitive measure for the SiO_2 thickness. In general, the measurement of more observables enables a more accurate characterization of the system. As previously shown,[16] different observables may be sensitive to different processes; thus, one can sometimes monitor and differentiate between several processes even though only a single characterization technique is applied.

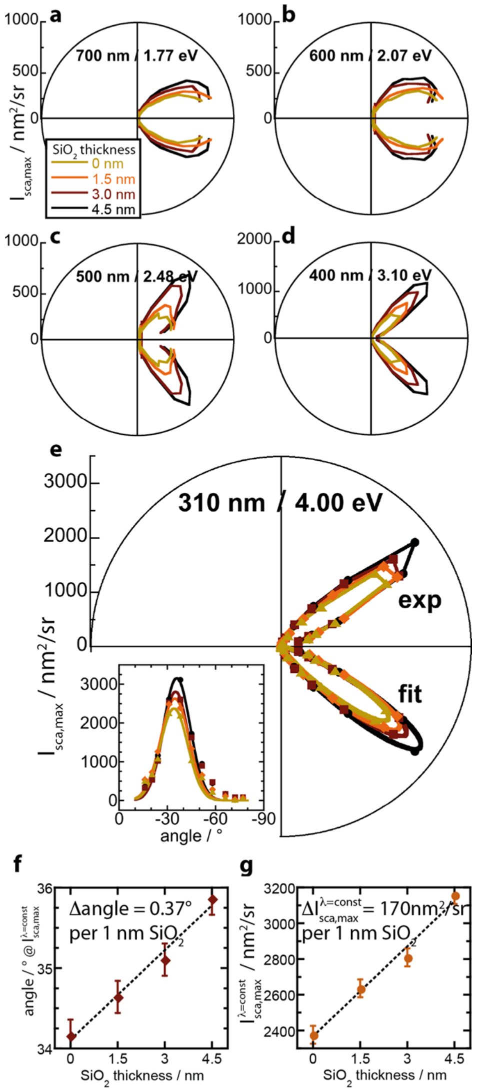

Figure 7. (a–d) Scattering patterns from Al nanoparticles covered with 0, 1.5, 3.0, and 4.5 nm of SiO_2 at different wavelengths. (e) Scattering pattern at 310 nm (4.00 eV). A Gaussian function has been fitted to the experimental data points. The inset shows the data points and the fit in Cartesian coordinates. (f) Shift of the angle at which $I_{sca,max}^{\lambda=const}$ occurs. (g) $I_{sca,max}^{\lambda=const}$ as a function of SiO_2 thickness.

Looking at the scattering patterns in Figure 7, we see that the addition of SiO_2 in general tends to increase the angular spread of the scattering patterns. As more SiO_2 is deposited, the maximum scattering angle increases and the scattering cross sections at large angles increase. This effect primarily originates from the single-particle level, but is aided by the fact that we have an ensemble of particles: In general terms, the reason behind the increase of scattering to larger angles is that addition of another material, with an index of refraction larger than 1, on top of the Al nanodisks, tends to shift all its multipolar resonances downward in frequency and to increase the mixing-in of higher multipole components to the field around the disk. This means that the scattering pattern will be less dipolar-like, *i.e.*, less concentrated in the forward direction around $\theta = 0°$. The fact that we have an ensemble of particles whose scattering signals interfere with each other, as described by the static structure factor, favors scattering into rather large angles, away from $\theta = 0°$ (*cf.* Figure 3). Thus, the ensemble of particles in a sense becomes a filter that tends to block scattering from the dipolar mode. In this context, it is, on the other hand, also worth pointing out that the deposition of a dielectric layer (SiO_2) on top of the particles, as well as the entire substrate, does not change the static structure factor determining the scattering cross section for a particular scattering angle, provided the scattering measurement is made in the same medium (air) as without the covering layer. The in-plane wave vector determining the static structure factor here is $|\vec{q}\,| = k \sin(\theta)$, with $k = \omega/c$, both with and without a layer of SiO_2.

The angular redistribution of scattered intensity also gives a clue to why we found a larger sensitivity to SiO_2 deposition in the scattering signal at a particular angle than in the extinction cross section. The extinction cross section is according to the optical theorem[8] set by scattering in all directions and absorption losses and therefore, here, shows less variation with the SiO_2 thickness.

CONCLUSIONS

In summary, we have studied the angular scattering patterns from Al nanoparticle ensembles formed by random sequential adsorption. We observe diffraction peaks, which are well reproduced theoretically by combining the single-particle scattering pattern with a structure factor describing the short-range order of the ensemble. In a proof-of-principle experiment we have also demonstrated that the sensitivity of nanoplasmonic sensing can be enhanced by looking at the scattered light from an ensemble of particles. In our experiment we coated the Al nanoparticles by SiO_2 of a thickness between 1.5 and 4.5 nm SiO_2. We obtained signal-to-noise ratios as high as 41 when monitoring the change of the maximum scattering cross section at a fixed angle, $I_{\text{sca,max}}^{\theta=\text{const}}$. This corresponds to an enhancement of ~70% compared to the traditional extinction measurements for sensing. The measurement of light scattered at a certain angle is thereby used to isolate those parts of the total scattered light that depends most sensitively on the SiO_2 layer thickness. In addition to an enhanced sensitivity, the measurement of the angular scattering patterns yields two new observables, namely, the scattering angle yielding a maximum in the cross section and this maximum scattering cross section at a fixed wavelength $I_{\text{sca,max}}^{\lambda=\text{const}}$. In this particular study, both turn out to be linearly dependent on the SiO_2 thickness.

This simple modification of traditionally performed nanoplasmonic sensing, *i.e.*, measurement of the extinction of the directly transmitted or reflected beam, to instead measure either scattered light at a fixed angle or the whole angular scattering pattern has proven to increase the sensitivity of the nanoplasmonic sensing experiment. Furthermore, the scattering peaks not only occur at the dipole resonance position but can be observed over a wide range of wavelengths. This may present a practical advantage when, for example, the LSPR peak in extinction falls into a spectral region that lies outside the range of the applied spectrometer or if parts of the measurement setup, substrate, or nanostructure are not transmitting or reflecting in this particular spectral region, thereby preventing the traditional sensing approach. Instead of making time-consuming or expensive changes to the measurement setup or sample structure, simply changing the angle of detection may solve the problem. The fact that the theoretical description of the scattering patterns is straightforward when the single-particle plasmonic properties and the particle positions in the ensemble are known (the latter can simply be obtained by SEM) opens the possibility of correlating theory and experiment established for single-particle[37] and extinction measurements.[16,31]

METHODS

Nanofabrication. Al nanoparticles have been fabricated by hole-mask colloidal lithography and e-beam lithography. Details about the fabrication process can be found in refs 28 and 30, respectively. The SiO_2 coatings have been deposited using a FHR MS150 sputter.

Extinction Measurements. The optical extinction spectra have been measured using a Varian Cary 500 double-beam spectrophotometer in the case of the spectra shown in Figure 1 and a Varian Cary 5000 spectrophotometer in the case of the spectra shown in Figure 5. The integration times in the Cary 500 and 5000 were 0.2 s. Since the Cary double-beam spectrophotometers measure one wavelength at a time, acquiring the whole spectrum takes, depending on the wavelength range, about 3 to 5 min.

Angle-Resolved Scattering Measurements. The experimental setup used to measure the scattering light is shown in Figure 1e. The light from a Xe arc lamp (75 W) is guided by an optical fiber (Ocean Optics Inc., 600 μm diameter, solarization-resistant; equipped with lens and aperture; thus, NA = 0.15) to the polarizer. Light hits the back of the substrate (opposite of where the Al nanoparticles are deposited) at normal incidence. Using the same kind of fiber, the scattered light is collected at a constant distance of 3 cm from the sample at different scattering angles θ in the plane spanned by the direction and the polarization of the incident light (*cf.* Figure 1e), and the intensity of the scattered light is measured by a UV–vis array spectrometer (Avantes AvaSpec-2048). The integration times varied between 0.1 to 3.5 s depending on the amount of scattered light at the respective angle and were then normalized to 1 s. As array spectrometers measure the whole wavelength range at the same time, this also corresponds to the time needed to record one spectrum. Using array spectrometers, one typically averages over several spectra in order to lower the S/N ratio. In this study, we averaged over 100 spectra; that is, the whole measurement took between 20 s and 6 min. Angles from $\theta = 16°$ to 77° off-normal have been measured. We obtain equivalent results for positive and negative angles. This is expected since the particle arrangement averaged over the illuminated area should be cylindrically symmetric. The particular angles shown in the angular plots of experimentally obtained data are 16.0°, 20.5°, 24.0°, 31.0°, 38.0°, 45.0°, 51.5°, 58.0°, 66.0°, 72.0°, and 77.0°. For angles smaller than 16°, the directly transmitted light beam makes the determination of the scattered light impossible. Setup limitations prevent the measurement of angles larger than 77°. The differential scattering cross section per particle has been calculated as

$$I_{\mathrm{sca}}(\lambda, \theta) = \frac{1}{\rho\Omega}\,\frac{\mathrm{counts}_{\mathrm{NP}}(\lambda, \theta) - \mathrm{counts}_{\mathrm{substrate}}(\lambda, \theta)}{\mathrm{counts}^{\mathrm{tra}}_{\mathrm{substrate}}(\lambda) - \mathrm{counts}_{\mathrm{dark}}(\lambda)} \qquad (4)$$

where λ is the wavelength of light, ρ is the particle density, Ω is the solid angle covered by the fiber in the measurement, and "counts" describes the number of photon counts of the detector with superscript "tra" referring to transmission geometry, *i.e.*, $\theta = 0°$. Subscript "NP" refers to a glass substrate with nanoparticles, "substrate" to a bare glass substrate, and "dark" to the measurement of the background/residue light when the incident light is blocked. Due to spectral limitations of the detector, the scattering pattern in this setup can be determined in the UV−vis spectral range between 950 and 280 nm (1.3−4.4 eV).

Calculations. The scattering patterns for a single nanodisk were calculated using a commercially available finite element method (Comsol Multiphysics 3.5a) together with Green's function method; for more details, see ref 38. The near field has been calculated using a finite element method from the same commercial software package (Comsol Multiphysics 3.5a).

Conflict of Interest: The authors declare no competing financial interest.

REFERENCES AND NOTES

1. Kreibig, U.; Vollmer, M. *Optical Properties of Metal Clusters*; Springer: Heidelberg, 1995.
2. Bohren, C. F.; Huffman, D. R. *Absorption and Scattering of Light by Small Particles*; Wiley: New York, 1998.
3. Sönnichsen, C.; Franzl, T.; Wilk, T.; von Plessen, G.; Feldmann, J.; Wilson, O.; Mulvaney, P. Drastic Reduction of Plasmon Damping in Gold Nanorods. *Phys. Rev. Lett.* **2002**, *88*, 077402-1–4.
4. Prikulis, J.; Svedberg, F.; Käll, M.; Enger, J.; Ramser, K.; Goksör, M.; Hanstorp, D. Optical Spectroscopy of Single Trapped Metal Nanoparticles in Solution. *Nano Lett.* **2004**, *4*, 115–118.
5. Lei, D. Y.; Appavoo, K.; Sonnefraud, Y.; Haglund, J.; Maier, S. A. Single-Particle Plasmon Resonance Spectroscopy of Phase Transition in Vanadium Dioxide. *Opt. Lett.* **2010**, *35*, 3988–3990.
6. Evanoff, D. D.; Chumanov, G. Size-Controlled Synthesis of Nanoparticles. 2. Measurement of Extinction, Scattering, and Absorption Cross Sections. *J. Phys. Chem. B* **2004**, *108*, 13957–13962.
7. Langhammer, C.; Kasemo, B.; Zorić, I. Absorption and Scattering of Light by Pt, Pd, Ag, and Au Nanodisks: Absolute Cross Sections and Branching Ratios. *J. Chem. Phys.* **2007**, *126*, 194702–11.
8. Langhammer, C.; Schwind, M.; Kasemo, B.; Zorić, I. Localized Surface Plasmon Resonances in Aluminum Nanodisks. *Nano Lett.* **2008**, *8*, 1461–1471.
9. Novotny, L.; van Hulst, N. Antennas for Light. *Nat. Photonics* **2011**, *5*, 83–90.
10. Shegai, T.; Brian, B.; Miljković, V. D.; Käll, M. Angular Distribution of Surface-Enhanced Raman Scattering from Individual Au Nanoparticle Aggregates. *ACS Nano* **2011**, *5*, 2036–2041.
11. Coenen, T.; Vesseur, E. J. R.; Polman, A.; Koenderink, A. F. Directional Emission from Plasmonic Yagi-Uda Antennas Probed by Angle-Resolved Cathodoluminescence Spectroscopy. *Nano Lett.* **2011**, *11*, 3779–3784.
12. Miljković, V. D.; Shegai, T.; Käll, M.; Johansson, P. Mode-Specific Directional Emission from Hybridized Particle-on-a-Film Plasmons. *Opt. Express* **2011**, *19*, 12856–12864.
13. Anker, J. N.; Hall, W. P.; Lyandres, O.; Shah, N. C.; Zhao, J.; Van Duyne, R. P. Biosensing with Plasmonic Nanosensors. *Nat. Mater.* **2008**, *7*, 442–453.
14. Schwind, M.; Zhdanov, V. P.; Zorić, I.; Kasemo, B. LSPR Study of the Kinetics of the Liquid-Solid Phase Transition in Sn Nanoparticles. *Nano Lett.* **2010**, *10*, 931–936.
15. Zhang, X.; Hicks, E. M.; Zhao, J.; Schatz, G. C.; Van Duyne, R. P. Electrochemical Tuning of Silver Nanoparticles Fabricated by Nanosphere Lithography. *Nano Lett.* **2005**, *5*, 1503–1507.
16. Schwind, M.; Langhammer, C.; Kasemo, B.; Zorić, I. Nanoplasmonic Sensing and QCM-D as Ultrasensitive Complementary Techniques for Kinetic Corrosion Studies of Aluminum Nanoparticles. *Appl. Surf. Sci.* **2011**, *257*, 5679–5687.
17. Langhammer, C.; Zorić, I.; Kasemo, B. Hydrogen Storage in Pd Nanodisks Characterized with a Novel Nanoplasmonic Sensing Scheme. *Nano Lett.* **2007**, *7*, 3122–3127.
18. Roy, D.; Fendler, J. Reflection and Absorption Techniques for Optical Characterization of Chemically Assembled Nanomaterials. *Adv. Mater.* **2004**, *16*, 479–508.
19. Aussenegg, F.; Brunner, H.; Leitner, A.; Lobmaier, C.; Schalkhammer, T.; Pittner, F. The Metal Island Coated Swelling Polymer over Mirror System (MICSPOMS): A New Principle for Measuring Ionic Strength. *Sens. Actuators, B* **1995**, *29*, 204–209.
20. Himmelhaus, M.; Takei, H. Cap-Shaped Gold Nanoparticles for an Optical Biosensor. *Sens. Actuators, B* **2000**, *63*, 24–30.
21. Stiles, R. L.; Willets, K. A.; Sherry, L. J.; Roden, J. M.; Van Duyne, R. P.Investigating Tip-Nanoparticle Interactions in Spatially Correlated Total Internal Reflection Plasmon Spectroscopy and Atomic Force Microscopy. *J. Phys. Chem. C* **2008**, *112*, 11696–11701.
22. Svedendahl, M.; Chen, S.; Dmitriev, A.; Käll, M. Refractometric Sensing Using Propagating *versus* Localized Surface Plasmons: A Direct Comparison. *Nano Lett.* **2009**, *9*, 4428–4433.
23. Kedem, O.; Vaskevich, A.; Rubinstein, I. Improved Sensitivity of Localized Surface Plasmon Resonance Transducers Using Reflection Measurements. *J. Phys. Chem. Lett.* **2011**, *2*, 1223–1226.
24. Kim, N.; Jung, W. K.; Byun, K. M. Correlation Analysis Between Plasmon Field Distribution and Sensitivity Enhancement in Reflection- and Transmission-Type Localized Surface Plasmon Resonance Biosensors. *Appl. Opt.* **2011**, *50*, 4982–4988.
25. Shegai, T.; Chen, S.; Miljković, V. D.; Zengin, G.; Johansson, P.; Käll, M. A Bimetallic Nanoantenna for Directional Colour Routing. *Nat. Commun.* **2011**, *2*, 481.
26. Shegai, T.; Johansson, P.; Langhammer, C.; Käll, M. Directional Scattering and Hydrogen Sensing by Bimetallic Pd-Au Nanoantennas. *Nano Lett.* **2012**, *12*, 2464–2469.
27. Svedendahl, M.; Käll, M. Fano Interference between Localized Plasmons and Interference Reflections. *ACS Nano* **2012**, *6*, 7533–7539.
28. Fredriksson, H.; Alaverdyan, Y.; Dmitriev, A.; Langhammer, C.; Sutherland, D.; Zäch, M.; Kasemo, B. Hole-Mask Colloidal Lithography. *Adv. Mater.* **2007**, *19*, 4297–4302.
29. Evans, J. Random and Cooperative Sequential Adsorption. *Rev. Mod. Phys.* **1993**, *65*, 1281–1329.
30. Zorić, I.; Zäch, M.; Kasemo, B.; Langhammer, C. Gold, Platinum, and Aluminum Nanodisk Plasmons: Material Independence, Subradiance, and Damping Mechanisms. *ACS Nano* **2011**, *5*, 2535–2546.
31. Sannomiya, T.; Scholder, O.; Jefimovs, K.; Hafner, C.; Dahlin, A. B. Investigation of Plasmon Resonances in Metal Films with Nanohole Arrays for Biosensing Applications. *Small* **2011**, *7*, 1653–1663.

32. Fraden, S.; Maret, G. Multiple Light Scattering from Concentrated, Interacting Suspensions. *Phys. Rev. Lett.* **1990**, *65*, 512–515.
33. Rojas-Ochoa, L. F.; Mendez-Alcaraz, J. M.; Saenz, J. J.; Schurtenberger, P.; Scheffold, F. Photonic Properties of Strongly Correlated Colloidal Liquids. *Phys. Rev. Lett.* **2004**, *93*, 073903–1−4.
34. Liew, S. F.; Forster, J.; Noh, H.; Schreck, C. F.; Saranathan, V.; Lu, X.; Yang, L.; Prum, R. O.; O'Hern, C. S.; Dufresne, E. R.; *et al*. Short-Range Order and Near-Field Effects on Optical Scattering and Structural Coloration. *Opt. Express* **2011**, *19*, 8208–8217.
35. Shegai, T.; Miljković, V. D.; Bao, K.; Xu, H.; Nordlander, P.; Johansson, P.; Käll, M. Unidirectional Broadband Light Emission from Supported Plasmonic Nanowires. *Nano Lett.* **2011**, *11*, 706–711.
36. Hanarp, P.; Käll, M.; Sutherland, D. S. Optical Properties of Short Range Ordered Arrays of Nanometer Gold Disks Prepared by Colloidal Lithography. *J. Phys. Chem.* **2003**, *107*, 5768–5772.
37. Hentschel, M.; Saliba, M.; Vogelgesang, R.; Giessen, H.; Alivisatos, A. P.; Liu, N. Transition from Isolated to Collective Modes in Plasmonic Oligomers. *Nano Lett.* **2010**, *10*, 2721–2726.
38. Miljković, V. D.; Shegai, T.; Johansson, P.; Käll, M. Simulating Light Scattering from Supported Plasmonic Nanowires. *Opt. Express* **2012**, *20*, 10816–10826.